Journal of Archaeological Science 145 (2022) 105646

Contents lists available at ScienceDirect

Journal of Archaeological Science

journal homepage: www.elsevier.com/locate/jas

3D visualization of bioerosion in archaeological bone

Kellie Sara Duffett Carlson [a,b,*,1], Kirsten Mandl [a,c,1], Ashley McCall [d], David Brönnimann [e], Maria Teschler-Nicola [a,f], Estella Weiss-Krejci [c,g], Brian Metscher [h]

[a] Department of Evolutionary Anthropology, University of Vienna, Austria, Djerassiplatz 1, 1030, Vienna, Austria
[b] Human Evolution and Archaeological Sciences, University of Vienna, Vienna, Austria
[c] Historical Archaeology, Austrian Archaeological Institute, Austrian Academy of Sciences, Franz-Klein-Gasse 1, 1190, Vienna, Austria
[d] Dublin, Ireland
[e] Integrative Prehistory and Archaeological Science, Department of Environmental Sciences, University of Basel, Spalenring 145, 4055, Basel, Switzerland
[f] Department of Anthropology, Natural History Museum Vienna, Burgring 7, 1010, Vienna, Austria
[g] Department of Social and Cultural Anthropology, University of Vienna, Universitätsstraße 7 (NIG), 1010, Vienna, Austria
[h] Department of Evolutionary Biology Unit for Theoretical Biology, University of Vienna, Djerassiplatz 1, 1030, Vienna, Austria

ARTICLE INFO

Keywords:
Bioerosion
microCT
Diagenesis
Taphonomy
Mortuary archaeology
Bone histology
Histotaphonomy

ABSTRACT

Palaeoradiology is increasingly being used in archaeological and forensic sciences as a minimally invasive alternative to traditional histological methods for investigating bone microanatomy and its destruction by diagenetic processes. To better understand ancient mortuary practices, taphonomic studies using microCT scanning methods are gaining an ever more important role. Recently it was demonstrated that 2D virtual sections obtained by microCT scanning of intact samples are comparable to physical sections for the rating and diagnosis of bioerosion in archaeological bone. Importantly, volume image data obtained from tomographic methods also allow the rendering and analysis of 3D models. Building on these methods we provide (1) detailed descriptions of bioerosion in 3D volume renderings, virtual sections, and traditional micrographs, and (2) accessible techniques for the visualization of bioerosion in skeletal samples. The dataset is based on twenty-eight cortical bone samples, including twenty femora (of which five are cremated), two ribs, two parietals, one mandibular ramus, one humerus, and two faunal long bones from five archaeological sites in Lower Austria dating from the Early Neolithic to the Late Iron Age. Notably, we reduce the need for time-consuming image segmentation by sequentially applying two noise-reducing, edge-preserving filters, and using an image-display transfer function that visualizes bioerosion, as well as Haversian and Volkmann canal structure and density in 3D. In doing so we are also able to visualize in 3D the invasion of canals by microbiota, which has previously only been reported in 2D sections. Unlike conventional thin sections, the 3D volume images shown here are easy to create and interpret, even for archaeologists inexperienced in histology, and readily facilitate the illustration and communication of microtaphonomic effects.

1. Introduction

To date most research on microscopic taphonomic alteration to bone has been performed using histology via light microscopy (LM) or scanning electron microscopy (SEM) (e.g., Garland, 1987; Grupe and Garland, 1993; Hackett, 1981; Turner-Walker and Jans, 2008; Turner-Walker, 2012). However, recent technical developments enable high-resolution, non-destructive 3D imaging of archaeological samples. X-ray computed microtomography (microCT or XRM) is increasingly being used as an alternative to conventional histological methods for the diagnosis of pathological alterations (Rühli et al., 2007), trauma (Baier et al., 2019), and diagenesis (Booth et al., 2016; Dal Sasso et al., 2014; Le Garff et al., 2017; Tripp et al., 2010, 2018) in modern and archaeological bone. Importantly, a strong correlation has been reported between virtual sections and histological micrographs for the evaluation of microbial bioerosion in ancient samples, along with a Virtual Histological

* Corresponding author. Department of Evolutionary Anthropology, University of Vienna, Austria, Djerassiplatz 1, 1030, Vienna, Austria.
E-mail addresses: kelliesard86@univie.ac.at (K.S. Duffett Carlson), kirsten.mandl@univie.ac.at (K. Mandl), amccall317@gmail.com (A. McCall), david.broennimann@unibas.ch (D. Brönnimann), maria.teschler@nhm-wien.ac.at (M. Teschler-Nicola), estella.weiss-krejci@oeaw.ac.at (E. Weiss-Krejci), brian.metscher@univie.ac.at (B. Metscher).
[1] These authors contributed equally to the research.

https://doi.org/10.1016/j.jas.2022.105646
Received 30 March 2022; Received in revised form 26 May 2022; Accepted 12 July 2022

Index (VHI) that can be used as an alternative to, or in conjunction with, indices developed for conventional microscopic methods (Mandl et al., 2022). While assessment of 2D virtual microCT sections using the VHI is sufficient for the rating and diagnosis of bioerosion, volume image data obtained from tomographic methods also allow the rendering and analysis of virtual models using commercially available software. This permits the visualization of microanatomy and bioerosion in 3D, providing a more non-destructive method for answering questions concerning postmortem history.

Importantly, the methodology provided here may facilitate the search for solutions to various problems in archaeological and forensic research. This includes, for example, the identification of bodies that have been subjected to some kind of mummification process (artificial or natural). This determination has so far been achieved by means of various invasive methods and techniques, including bone histology (e.g., Booth et al., 2015; Parker Pearson et al., 2005) and chemical analysis (e.g., Ghezal et al., 2019). A related question concerns that of the burial environment. A persistent matter of disagreement is the origin of osteolytic microbiota and how they gain access to bone. Some hypothesize endogenous induction by the enteric microbiome (e.g., Bell et al., 1996; Booth, 2016; Booth et al., 2016; Bronnimann et al., 2018; Hollund et al., 2012; White and Booth, 2014), while others suggest an exogenous origin from the burial environment (e.g., Kendall et al., 2018; Kontopoulos et al., 2016; Metcalf et al., 2016; Turner-Walker, 2019). As it is expected that exogenous initiation would progress from the periosteum inward, three-dimensional assessment of samples that incorporates both a (semi)quantitative index (e.g., the VHI) of the full virtual stack, and visualization of volume renderings, will help track the progress of microbial alteration to identify an endosteal or periosteal origin in samples with inhibited bioerosion.

2. Background

MicroCT is a non-destructive imaging procedure that computes a stack of cross sections through an object from a series of 2D radiographic projections. This 3D volume dataset is composed of volumetric pixels (voxels), each of which has a specific grey-scale value representing local X-ray attenuation, as well as accurate size calibration (Withers et al., 2021). The microfocus X-ray tubes used in lab-based microCT scanners provide excellent image resolution, down to a few microns or lower, which permit the accurate description of the minute physical properties of both the internal and external skeleton (Moore, 2013; Scherf, 2013), generally without causing tissue damage (e.g., DNA degradation: Walton et al., 2015). Objects such as bone, which have inherently high X-ray absorption, can be imaged without special preparation. Most commercial lab-based microCT systems can accommodate samples up to 100–200 mm in length and 5–10 mm in diameter for high-resolution scans, and so can produce high-resolution images of smaller bones or fragments. Larger bones can be imaged with lower resolutions (e.g., 10–50 μm voxel sizes) using larger systems (Withers et al., 2021).

Dal Sasso et al. (2014) and Booth et al. (2016) were amongst the first to use lab based-microCT sections to assess bioerosion in archaeological samples. Recently Tripp et al. (2010, 2018) applied a Gaussian filter to microCT images to assess cortical porosity in relation to collagen preservation, while Caruso et al. (2020, 2021) used synchrotron radiation microCT (SR-microCT) to identify diagenesis in modern and ancient remains; this included the creation of segmented volume renderings to visualize vascular and canal networks, as well as micro-porosity with a 3D median filter (following Cooper et al., 2003). Neither assess the 3D volumes for the presence of osteolytic bacteria-induced microscopic focal destruction (MFD) (see Balzer et al., 1997; Child, 1995; Hackett, 1981; Jans et al., 2004; Jans, 2008). Dal Sasso et al. (2014) and Booth et al. (2016) created unfiltered grey-scale volume renderings to visualize microtaphonomy. Though innovative at the time, these volume renderings can be improved upon by the use of noise-reducing, edge-preserving filters, and visualizing the data with a carefully chosen image display transfer function (colormap) that readily differentiates between unaltered bone and demineralized, bioeroded bone.

We describe bioerosion in a selection of 3D volume renderings, virtual sections, and traditional micrographs. Notably, we reduced the need for time-consuming image segmentation by the consecutive application of the Bilateral and Sobel filters, and using the glow.col colormap, which provides, via artificial shading, increased contrast range to better visualize bioerosion, and canal structure and density in 3D. As the study of taphonomic processes becomes increasingly important in bioarchaeological research, refinement of histological methods, and a better understanding of postmortem changes at the microstructural level are called for. The aim of the present paper is thus to provide an accessible methodology for the 3D visualization of bioerosion using virtual anthropology techniques.

3. Material and methods

The dataset is based on twenty-eight cortical bone samples (twenty femora, two ribs, two parietals, one humerus, one mandibular ramus, and two faunal long bones) from five archaeological sites in Lower Austria (for further details see Supplementary Material S1). Seven human samples derive from the Early Neolithic (Linear Pottery) site of Asparn-Schletz, six from the Early Bronze Age site of Gemeinlebarn A, four from Late Bronze Age Inzersdorf ob der Traisen, seven samples (one faunal and four human) from Late Iron Age Göttlesbrunn, and four (one faunal) from Late Iron Age Roseldorf (see Mandl et al., 2022). The individuals from Gemeinlebarn, Inzersdorf ob der Traisen, and Göttlesbrunn were excavated from prehistoric cemeteries (Fritzl, 2017; Karwowski and Czubak, 2019; Szombathy, 1929, 1934). The sites of Asparn-Schletz and Roseldorf are ancient settlements. In the case of Asparn-Schletz the finds derive from graves, large ditches, and different levels of a structure 8 m deep, considered to be a well (Pieler and Teschler-Nicola, 2019; Windl, 1998, 2009). The human and faunal remains from Roseldorf were recovered at two Iron-Age sanctuaries and a sacrificial pit (Holzer, 2009, 2010a,b; Teschler-Nicola, 2017; Trebsche, 2020). It has been debated for Roseldorf whether the human individuals in sanctuaries were defleshed and disarticulated perimortem, or if they constitute bones that were reburied after the soft tissues had decayed (Holzer, 2010a; Teschler-Nicola, 2017; for French contemporaneous sites cf. Ghezal et al., 2019).

Using a diamond wheel blade attached to a Dremel® 3000 electric drill, samples 1–2 cm thick were extracted from the anterior aspect of the proximal femoral diaphysis (n = 15) inferior to the surgical neck. Skull (n = 2), rib (n = 2), humerus (n = 1), and mandible (n = 1) fragments were also sampled, as were cremated long bones (n = 5), and faunal mammalian long bones (n = 2) (Supplementary Material S1). The samples were previously assessed with the Oxford Histological Index (OHI) (Hedges et al., 1995; Millard, 2001) and Virtual Histological Index (VHI) by Mandl et al. (2022). All figures were formatted using GIMP software (v. 2.99.6), and the ScientiFig plugin (Aigouy and Mirouse, 2013) for Fiji software (Schindelin et al., 2012).

3.1. Light microscopy (LM) and scanning electron microscopy (SEM)

Twenty-four of the twenty-eight samples were embedded in a two-compound resin (Biodur® E1/E2) according to a protocol for undecalcified bone (Schultz, 2001) (Supplementary Material S2). Using a Leica SP 1600 saw-blade microtome (Leica Microsystems) the resin blocks were sectioned along the transverse plane to a thickness ranging from 30–60 μm, mounted to a glass slide with Histokitt (ROTI®), then covered with a glass cover slip. Micrographs were taken with a DS-Ri2 camera (Nikon) mounted to a Nikon Eclipse Ni light microscope with 4 ×, 10 ×, and 20 × magnification under plane light, polarized light (XPL), and differential phase contrast light. To visualize collagen a lambda plate was used with XPL. All visualizations were conducted with NIA Elements BR Software (Nikon). Six samples were mounted on

carbon planchets and examined with an IT 300 LAB6 (JEOL Ltd.) scanning electron microscope at low vacuum at 25.0 kV under high magnification. Images were taken in backscatter electron mode (see Mandl et al., 2022).

3.2. X-ray microtomography (microCT)

The same samples used for LM and SEM (intact bone or embedded blocks) were mounted in plastic cylinders supported with synthetic foam then microCT scanned at the University of Vienna Theoretical Biology imaging lab using a Zeiss/Xradia MicroXCT-200 or a Bruker/Skyscan 1272 system with image resolutions ranging from 4–10.9 μm (isotropic voxel size) (see Mandl et al., 2022 and Supplementary Material S2).

3.3. Image visualization

Entire reconstructed image stacks were visualized with the Amira software (v. 2020.2, Thermo Fisher Scientific). Samples were rotated to align the entire stack in the transverse plane, the direction in which virtual cross-sections were visualized. Two built-in edge-preserving filters were applied sequentially to the dataset, both of which function to reduce noise and detect edges. First, the Bilateral filter was applied in the direction of the canals (kernel size = 5; similarity = 20) for balancing smoothing while maintaining sharp edges (such as canals and MFD). Second, the Sobel filter was applied to the Bilateral filtered dataset; this step enhances intensity gradients, emphasizing important structural properties.

The composite filtered dataset was visualized as a 3D volume image using the Volume Rendering module. A volume rendering creates an image of a 3D dataset without segmentation by simulating the casting of light rays through the volume by assigning transmission and absorption parameters to each voxel (Schroeder et al., 2018; Thermo Scientific™, 2018). In doing so the density information of the dataset is retained, unlike in an isosurface, which permits the visualization of important topographical details (Ryan and Sukhdeo, 2016), such as textured canals and bioerosion. Edge 3d and Edge 2d were selected for Shade Effects with the Lighting set to None. The volume renderings were visualized using the glow.col colormap, which is packaged in the Amira software.

Initially the volume renderings were visualized using two built-in colormaps: (1) volrenWhite.am, and (2) glow.col. Colormaps determine the transparency and color values with which to display the image grey-scale values (Schroeder et al., 2018). The “white” colormap, for which intensity gradients below the colormap port minimum are rendered transparent, was found to be less informative than the “glow” colormap. The artificial shading and edge coloring of the latter provides a good contrast range (Handschuh et al., 2010; Ryan and Sukhdeo, 2016), and a relative color scale that permits the visualization and differentiation of the densest (yellow), unaltered bone from the least dense (red), demineralized, bioeroded bone. More specifically, as sequential application of the filters allows the detection of edges (i.e., those of anatomical canals and bacterial endocasts), it is possible to visualize unaffected, healthy bone (which presents as transparent void), healthy canals (which present as yellow), and bacterial endocasts (red channels or trails along the walls of canals). It should be noted that care must be taken when adjusting the colormap, as over-adjustment can result in misleading visualizations.

An open access equivalent of the “glow” colormap can be found for Fiji/ImageJ as the “glow” Lookup Table. Similarly, the Bilateral and Sobel filters or their formulae (Tomasi and Manduchi, 1998; Burger and Burge, 2013), and other edge-preserving and/or noise-reducing filters (e.g., Mean Shift, Kuwahara) are also implemented in open access software, such as Fiji/ImageJ as plugins/.jar files.

4. Results

Five samples were selected from the dataset to demonstrate how bioerosion is visualized in 3D volume renderings in comparison to virtual cross-sections and thin section micrographs. These samples (all human) derive from femora from Graves 2 and 5 of Göttlesbrunn (GÖ04 and GÖ01), a humerus from the upper part of the alleged Asparn-Schletz well (SB02), a femur from Gemeinlebarn Grave A32 (GE08), and a cremated long bone fragment (possible femur) from Roseldorf, Sanctuary Object 30, District 2 (R01). Further images can be found in the Supplementary Material (S3–S30).

4.1. GÖ04/femur (OHI 5/VHI 5) (Fig. 1)

Micrographs: No microscopic focal destruction (MFD) can be found in the entire thin section. Many osteocyte lacunae resemble fresh bone in their shape and condition; however, the majority display enlarged canaliculi indicative of Wedl tunneling Type 2 (Supplementary Materials S3a). A minority of Haversian canals are filled with exogenous mineral precipitation that was not further identified. The circumferential lamellae of the periosteal layer are eroded while a layer of sediment covers the endosteal surface. There is a superficial area of brown staining along the periosteal surface. Collagen content is very good with weaker birefringence in areas along the midline and towards the periosteum (Supplementary Materials S3b). There is a small concentration of microfissures along the endosteal layer that follow the anatomy of a small number of osteons (Supplementary Materials S3c).

Virtual cross-sections: The bone is in nearly perfect condition with no bioerosion, only microfissures originating from the endosteal and periosteal surfaces, some of which travel around or through the individually visually undifferentiated concentric lamellae towards the midline, as seen in the thin sections. These visually undifferentiated lamellae are distinct, and grey values remain consistent throughout and between virtual slices through the 3D image. The endosteal and periosteal circumferential lamellae, which are also visually undifferentiated, have flaked off; matrix with higher density inclusions is attached to the surfaces with some infilling of canals as described in the thin sections.

Volume rendering: Canals are abundant, clearly defined, and more yellow than red, though not as yellow as canals of other unaffected samples. This likely results from the lower mineralization (lower density) associated with the younger age of this specimen (late juvenile) in comparison to, as will be seen, SB01 (Supplementary Material S4), a late adult found in the lower part of the alleged well of Asparn-Schletz. The canals in sample GÖ04 are surrounded by transparent void. The periosteal and endosteal borders are ragged where the circumferential lamellae have flaked off.

4.2. GÖ01/femur (OHI 4.5/VHI 4.5) (Fig. 2)

Micrographs: The section is mildly affected by bioerosion with the highest concentration of MFD present along the midline. Osteocyte lacunae are numerous. The circumferential lamellae are free of MFD. Overall collagen content is very high (Supplementary Material S5). Bacterial attack is concentrated primarily around and along the walls of the Haversian and Volkmann canals; these areas also have the highest concentration of enlarged canaliculi, indicative of Wedl Type 2 tunneling. The periosteal surface is heavily eroded with brown staining along the periphery. Microfissures penetrate the bone from the periosteum, following the microanatomy. Microfissures are also present along the endosteal surface.

Virtual cross-sections: Bioerosion is minimal. Grey values are mostly consistent throughout and between individual virtual slices; however, there is some loss of density (darker grey values), particularly along the midline. The visually undifferentiated lamellae surrounding Haversian canals are distinct, but MFD is present in the form of small perforations clustering around the Haversian and Volkmann canals, and within the concentric lamellae, particularly along the midline. The smaller MFDs cluster to form larger MFDs. There is reduced density surrounding some canals. The inner and outer circumferential lamellae

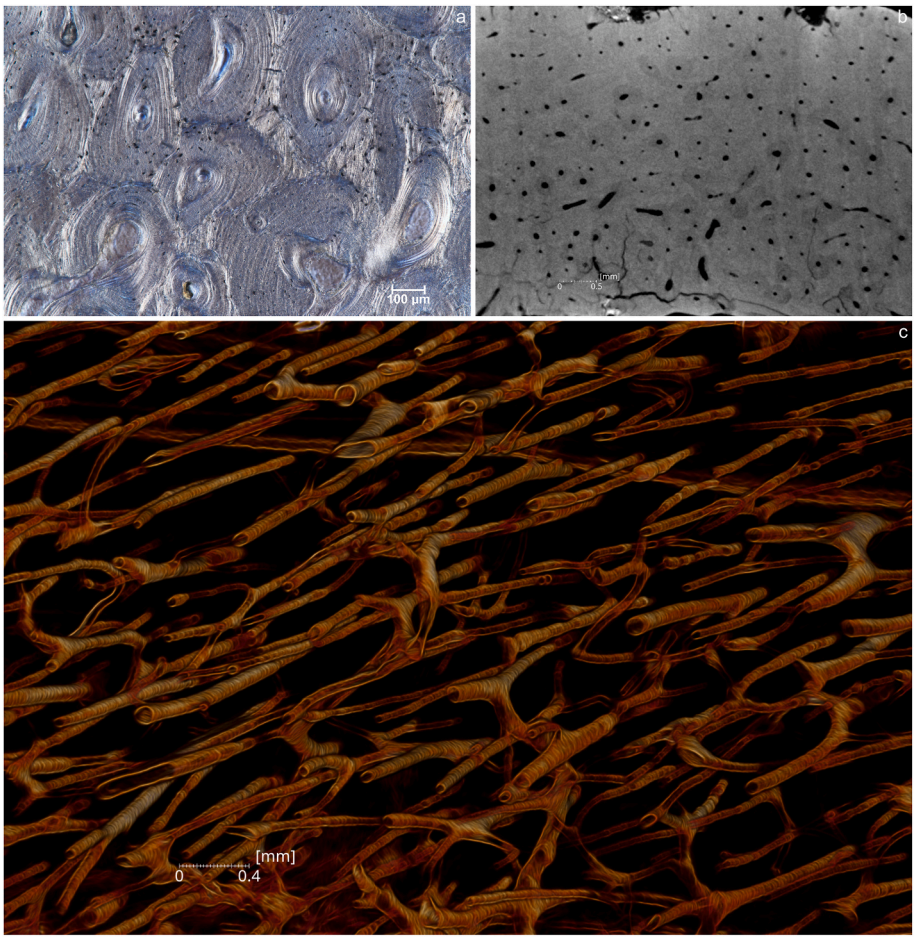

Fig. 1. Sample GÖ04 (Göttlesbrunn), a late juvenile female. (a) Light micrograph of midline of a transverse histological thin section (interference phase contrast under 10(1 ×) magnification). (b) Single virtual transverse cross-section (1 voxel [6.7 µm] thick) through a microCT image showing midline and periosteal surface. (c) 3D volume rendering with the "glow" colormap of entire virtual dataset showing midline.

are eroded.

Volume rendering: The canals are smooth and yellow but are surrounded by small, orange-red thread-like clusters of MFD; upon zooming into the canals, thin areas of reduced density that present as reddish trails can be seen traversing the length of the yellow canals. These threads of bioerosion can be seen encircling and passing between canals. There are small perforations to some of the canals. Bioerosion clusters in the midline, though much void remains.

4.3. SB02/humerus (OHI 2.5/VHI 2.5) (Fig. 3)

Micrographs: Bioerosion is inhibited. Areas remain unaffected with good preservation of the microstructure, particularly along the endosteal surface. However, there is MFD throughout the entire section, and most of the lacunae are enlarged. Collagen preservation is moderate to good (Supplementary Material S6). Microfissures follow the microanatomy, primarily along the periosteal surface, with one running through the entire section. Almost all the canals are filled with exogenous mineral precipitation. Both the periosteal and endosteal surfaces are strongly eroded.

Virtual cross-sections: The bone has undergone bioerosion in large irregular patches. Canals are present throughout the virtual stack; the visually undifferentiated circumferential lamellae of the periosteal and endosteal surfaces have been shed. Bioerosion is present along the midline towards the periosteum more so than the endosteum. Large patches of bioerosion present as darker grey values; in these regions visually undifferentiated concentric lamellae are difficult or impossible to distinguish. In areas where bioerosion is inhibited, MFD can be distinguished and visually undifferentiated concentric lamellae remain visible. There is a thin microfissure moving from the endosteum into the midline.

Volume rendering: Canals are still present, but their quality varies between regions analogous to what is found in the virtual cross-sections. The canals to the right and towards the endosteum are denser (more yellow) than those to the left of the image. However, the better-preserved canals are patched with red, and it is difficult to clearly visualize their interiors. The canals that have undergone heavier microbial attack are less dense, redder, and withered. It is difficult to distinguish the eroded anatomical canals from microbial tunneling. Although the circumferential lamellae have been heavily eroded, the layer that remains is still relatively dense (yellower), though patched with red. Some void remains, particularly towards the right.

4.4. GE08/femur (OHI 0.5/VHI 0.75) (Fig. 4)

Micrographs: The bacterial attack is heavy throughout much of the section except for the periosteal surface. There is yellow staining along the periosteum along with enlarged canaliculi and lacunae. There is some remaining collagen in this area (Supplementary Material S7). The midline to the endosteal surface is heavily eroded. There is also some yellow staining along the endosteal surface. MFD is present along the circumferential lamellae. There are two embedding artefacts. Only Haversian canals are identifiable.

Virtual cross-sections: The bone has undergone bioerosion in large irregular patches. Anatomical canals remain but bioerosion is pervasive

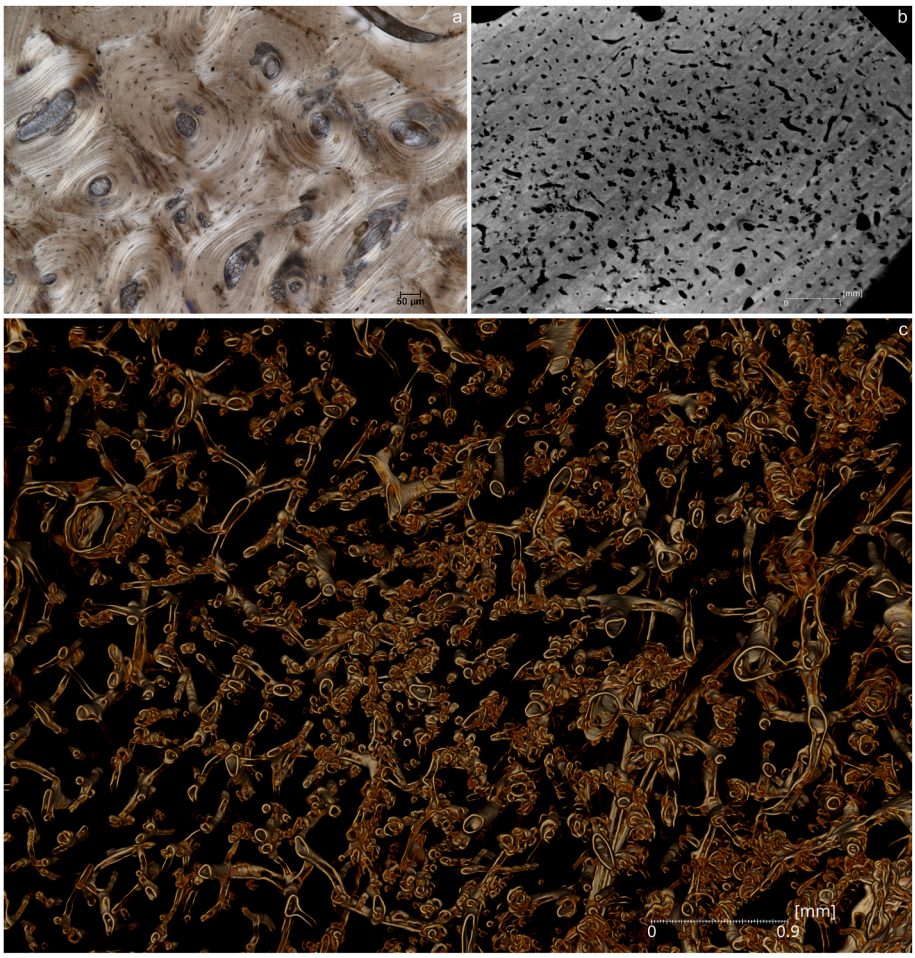

Fig. 2. Sample GÖ01 (Göttlesbrunn), an early adult female. (a) Light micrograph of midline of a transverse histological thin section (polarized light and under 10(2 ×) magnification). (b) Single virtual transverse cross-section (1 voxel [8.0 µm] thick) through a microCT image showing midline, and periosteal and endosteal surfaces. (c) 3D volume rendering with the "glow" colormap of entire virtual dataset showing midline.

throughout and between virtual slices. Only the smallest islands and trails of unaffected bone remain; the bioerosion is now so heavy that individual MFDs cannot be distinguished. Lamellae surrounding Haversian canals, which are visually undifferentiated, can only be distinguished from the surrounding interstitial lamellae because they have been, presumably, preferentially attacked by bacteria and thus present as thick rings of darker grey values. Both the periosteal and endosteal circumferential lamellae have been sloughed. Embedding artefacts travel transversely along a section of the periosteum, as noted in the histology.

Volume rendering: As found in the virtual sections, bioerosion is pervasive throughout the sample. It is difficult to discern anatomical canals from microbial tunneling; both are visualized as red channels surrounded by fibrous red webs. Slightly less affected, slightly more yellow canals can be recognized towards the left of the image.

4.5. R01/cremated long bone (OHI 5/VHI 4.5) (Fig. 5)

Micrographs: Thermally induced diagenetic alteration is visible throughout the entire section, resulting in a heterogeneous matrix characterized by a loss of the lamellar structure. No MFD is visible. Collagen preservation is moderate along the endosteal surface (Supplementary Material S8). Osteocyte lacunae are also well-preserved.

Virtual cross-sections: The grey values are a consistent light-medium grey throughout the stack. The visually undifferentiated lamellae are thicker along the endosteum than periosteum. There may be some evidence of bioerosion just below the periosteal layer adjacent to the microfissures. Canals are evident throughout, though they appear smaller than usual; burning at medium-to-high/high temperatures has been shown to result in shrinkage, cracking, and crystallization (Boschin et al., 2015; Ellingham and Sandholzer, 2020; Hanson and Cain, 2007). There are a small number of fine microfissures penetrating the periosteum. In some areas visually undifferentiated lamellae surrounding Haversian canals remain visible, perhaps due to what are tentatively identified as cement lines that are just vaguely visible around some Haversian systems.

Volume rendering: Although there is some demineralization caused by burning, there is little evidence for MFD, save perhaps just below the periosteal surface. The canals are clear and well defined while the void between them remains clear of bioerosion.

5. Discussion

5.1. Comparison with previous methods

The volume rendering depictions of bacterial attack are worth particular mention as we were able, using the "glow" colormap, to visualize in 3D what has previously only been reported in 2D. It is hypothesized that bacteria disseminate through and enlarge the canalicular network, accessing collagen via Haversian and Volkmann canals (Hackett, 1981; Kendall et al., 2018; Turner-Walker, 2019). Turner-Walker (2012) and Yoshino et al. (1991) also describe the occupation of Haversian canals by bacteria. While it was not possible to visualize bacterial attack on the canalicular network in these microCT images due

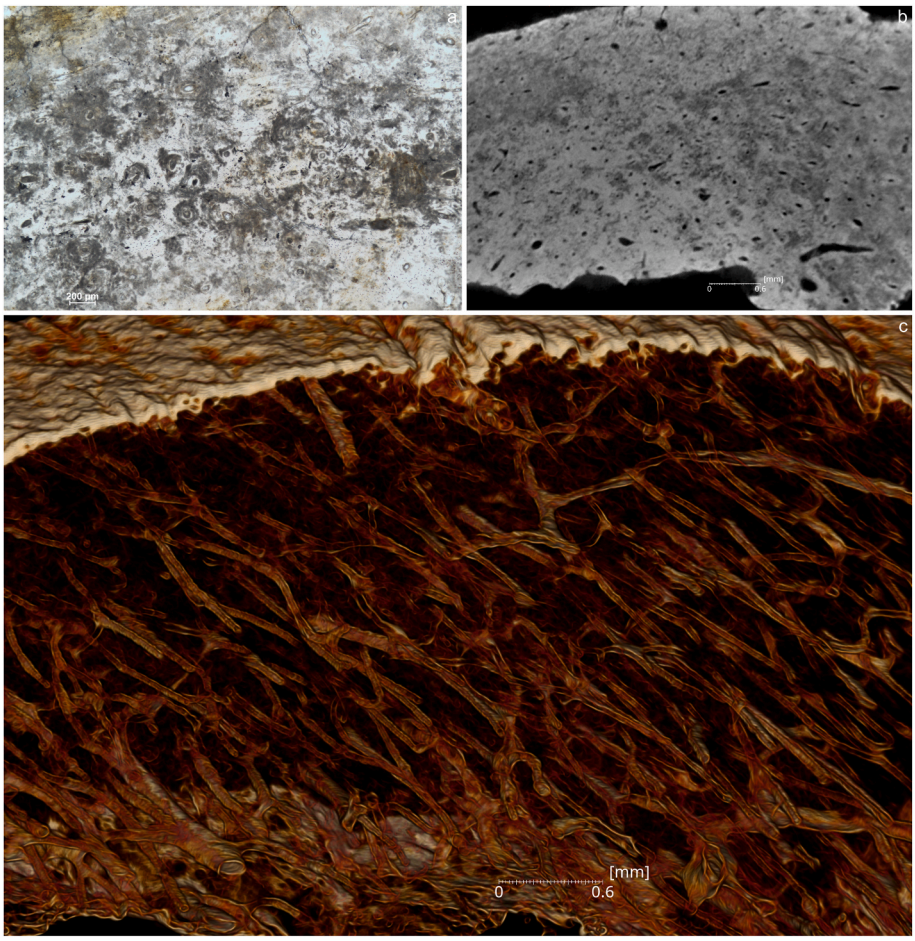

Fig. 3. Sample SB02 (Asparn-Schletz), a juvenile of unknown sex. (a) Light micrograph of midline of a transverse histological thin section (plane light and under 4(1 ×) magnification). (b) Single virtual transverse cross-section (1 voxel [8.0 µm] thick) through a microCT image showing midline, and periosteal and endosteal surfaces. (c) 3D volume rendering with the "glow" colormap of entire virtual dataset showing midline, and periosteal and endosteal surfaces.

to restrictions imposed by scan resolution (Mandl et al., 2022), we detected evidence of bacterial attack within the canals. Sample GÖ01 (Fig. 6) provided a particularly interesting volume in which fine red trails follow the interior length of well-preserved yellow canals, the colors reflecting differences in X-ray density. We interpret these as the traces of bacteria that have entered the Haversian and Volkmann canals, consumed their soft tissues (i.e., blood and lymphatic vessels, and nerve fibers), and attacked the more mineralized concentric and interstitial lamellae, leaving trails of reduced mineralization behind. Indeed, we see further evidence of bioerosion in the form of miniscule holes that penetrate some canals (Fig. 6), and as endocasts of bacteria which take the form of narrow, almost translucent red tunnels through the bone matrix. Jackes et al. (2001) also described what they believe to be the endocasts of bacterial chains as varied trajectories of circumscribed tunnels, visible in both longitudinal- and cross-sections. These tunnels present in volume renderings, for example the femur from Gemeinlebarn Grave A21 (GE15, Supplementary Material S9), as thin red channels that migrate through the bone, often in the direction of the Haversian canals, but also in numerous directions. Depending on the severity of the erosion, they may present as discrete spiral-like red tunnels distinct from the anatomical canals, to an almost cobweb-like film that veils degraded canals (e.g., SB02, Fig. 3), or even as an amorphous spongy texture (e.g., GE08, Fig. 4) in the most poorly preserved samples.

Jackes et al. (2001) also noted that in previously published figures (e.g., Bell, 1990; Garland, 1987; Grupe and Dreses-Werringloer, 1993; Hackett, 1981; Piepenbrink, 1986; Schultz, 1986) illustrating MFD, the magnification was not high enough to clearly visualize bioerosion, and that the cross-sections these authors used resulted in a view that resembles grape clusters, which does not match what can be visualized using longitudinal sections, such as those published by Bell (1990). These grape-like clusters are also visible in the 3D volume of GÖ01 (see Fig. 6). When the volume is viewed from different angles it can be seen that these clusters are actually tunnels that run longitudinally and at angles through the bone (Fig. 7). This visualization is similar to, but clearer than what is seen at very high magnification (>600 ×) with microscopy.

MicroCT is a valuable tool in this respect, as it permits the selection and visualization of any location within a sample in any orientation. Samples scanned, for example, in the coronal (or any oblique) plane, can be virtually resliced to the transverse plane. The virtual dataset can also be rotated to align with any anatomical plane using landmarks. We chose to virtually reslice our samples for assessment in the orientation of traditional thin sections: (1) to facilitate comparison with traditional micrographs, and (2) because 3D visualization of the canals and erosion in planes that do not follow the orientation of the Haversian systems made it difficult to assess bioerosion patterns in a three-dimensional sample. Furthermore, samples can be virtually cropped to visualize smaller volumes. The capacity to reslice, rotate, and virtually crop or dissect samples, repeatedly if desired, is specifically achievable with virtual but not conventional histologic methods.

5.2. *Effects of skeletal sample region*

While the femoral diaphysis, which has a thick cortical layer, is

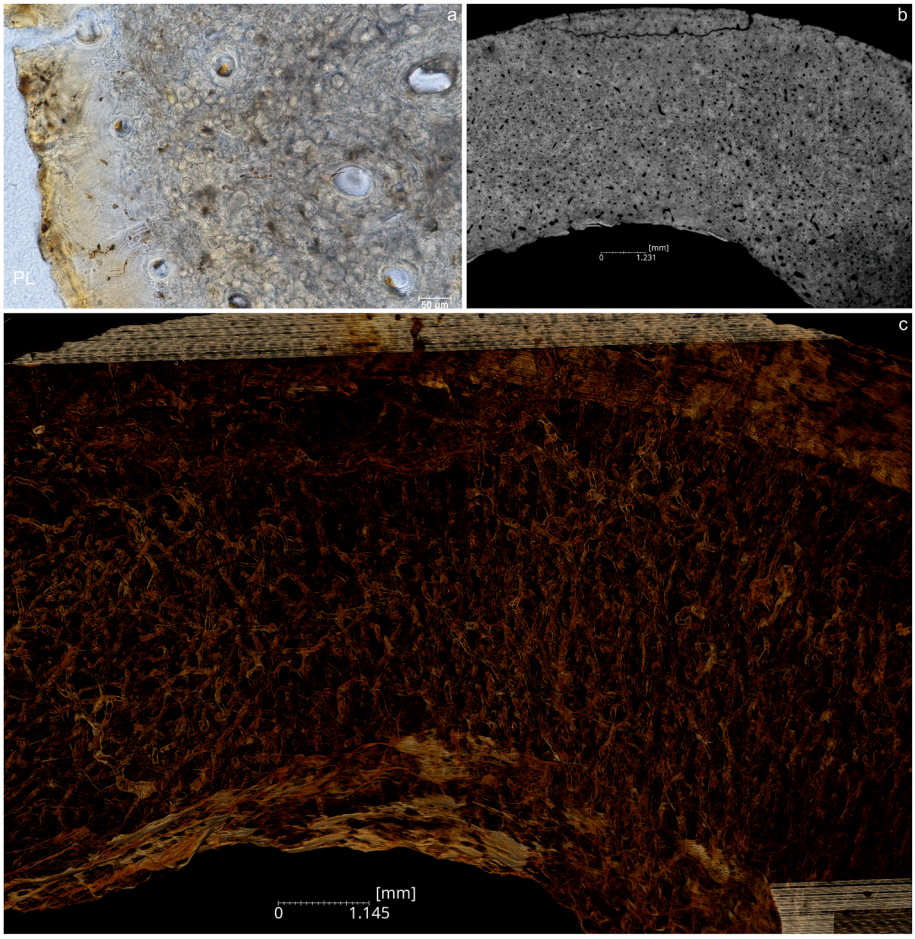

Fig. 4. Sample GE08 (Gemeinlebarn), a mature male. (a) Light micrograph of midline and periosteal surface of a transverse histological thin section (plane light and under 20(1 ×) magnification). (b) Single virtual transverse cross-section (1 voxel [8.0 µm] thick) through a microCT image showing midline, and periosteal and endosteal surfaces. (c) 3D volume rendering with the "glow" colormap of entire virtual dataset showing midline and endosteal surface.

preferred for visualizing canal structure and Haversian systems, our research shows that bioerosion can also be visualized in mandibular (Supplementary Material S4), cranial (Supplementary Material S10 & S11), and rib (Supplementary Material S12 & S13) samples. However, some volume renderings can be more difficult to interpret. For example, mandibular sample SB01 from the lower part of the Asparn-Schletz well (Supplementary Material S4), an OHI/VHI 5, has numerous anatomical canals that can be clearly visualized within the void, while subadult cranial sample SB04 from the same part of the same well (Supplementary Material S10)—also an OHI/VHI 5—which has fewer canals, is not so clearly visualized. Sample R02 from a large sacrificial pit (Object 14, District 1) at Roseldorf (Supplementary Materials S11) (OHI/VHI 2), also a cranial fragment, but this time of an adult, provides a clearer image; however, there is higher density exogenous mineral precipitation around the canals and trabeculae of this sample, which facilitates visualization. Humeral fragment SB02 (Fig. 3) (OHI/VHI 2.5) of a juvenile with numerous canals also provides a clear visualization. Rib samples from Göttlesbrunn Grave 5/GÖ24 (Supplementary Material S12) (OHI/VHI 4.5) and Grave 2/GÖ25 (Supplementary Material S13) (OHI 4/VHI 5), which have numerous canals (particularly GÖ24), can be clearly visualized but are not as easy to interpret as femoral samples. In short, the 3D visualization of unburnt femora, cranial elements, and ribs can provide easily readable images of taphonomic changes in bone microstructure, as it can illustrate the degree of deterioration of the Haversian and Volkmann canals.

5.3. Effects of cremation

It has been suggested that some cremated samples can be evaluated with the VHI, though the degree of burning may affect how easily this can be done (Mandl et al., 2022). Interestingly, we found that although microanatomy could still be visualized in virtual sections, even if poorly, the volume renderings of cremated samples were often but not always extremely poor, even in instances of an OHI 5/VHI 4.5. Sample R01 (Fig. 5) provided a significantly clearer 3D visualization than IN02 (Supplementary Material S14), IN03 (Supplementary Material S15) or IN04 (Supplementary Material S16). Specific calibration of the microCT scans to measure absolute mineral density, or more particularly calcium content, may help to better visualize cremated remains (Handschuh et al., 2017). Lastly, previous research suggests that cremation results in bone shrinkage, cracking, and crystallization (Boschin et al., 2015; Ellingham and Sandholzer, 2020; Hanson and Cain, 2007). While we are able to visualize dense (bright white) calcite in the scans, as well as cracking, morphometric analysis is required to confirm shrinkage.

5.4. Effects of pathological alteration

With any histological evaluation, familiarity with microanatomical structures is required to identify their presence and destruction by bioerosion. It is also useful to have an understanding of, for example, hematologic and metabolic bone diseases, and how they are visualized in microCT images. Pathological alterations affect the visualization and interpretation of skeletal remains, including, we found, in volume

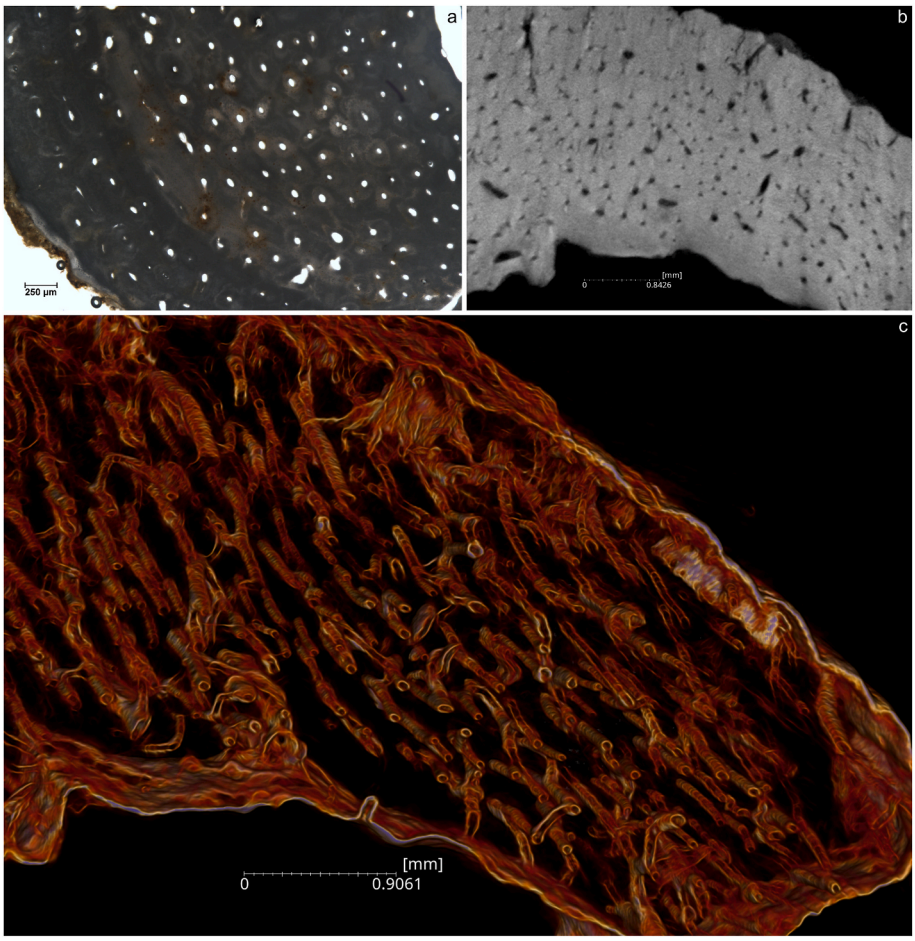

Fig. 5. Sample R01 (Roseldorf), an adult of unknown sex. (a) Light micrograph of midline, periosteal and endosteal surfaces of a transverse histological thin section (plane light and under 4(1 ×) magnification). (b) Single virtual transverse cross-section (1 voxel [8.5 µm] thick) through a microCT image showing midline, and periosteal and endosteal surfaces. (c) 3D volume rendering with the "glow" colormap of entire virtual dataset showing midline, periosteal and endosteal surfaces.

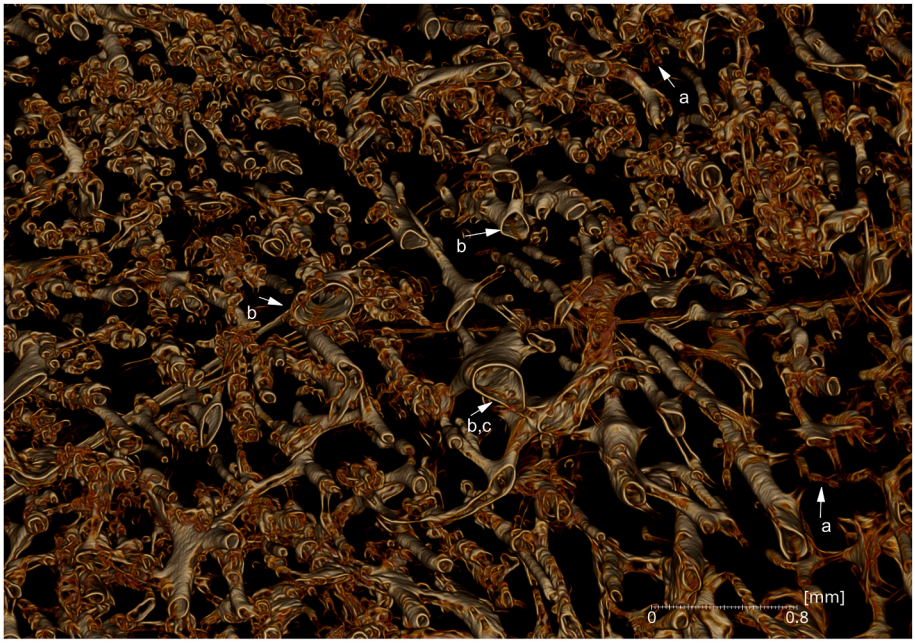

Fig. 6. 3D volume rendering with the "glow" colormap showing MFD tunneling (a), red trails of bioerosion (b) and miniscule holes in Haversian canals (c) in midline of femoral sample GÖ01 (Göttlesbrunn). (For interpretation of the references to color in this figure legend, the reader is referred to the Web version of this article.)

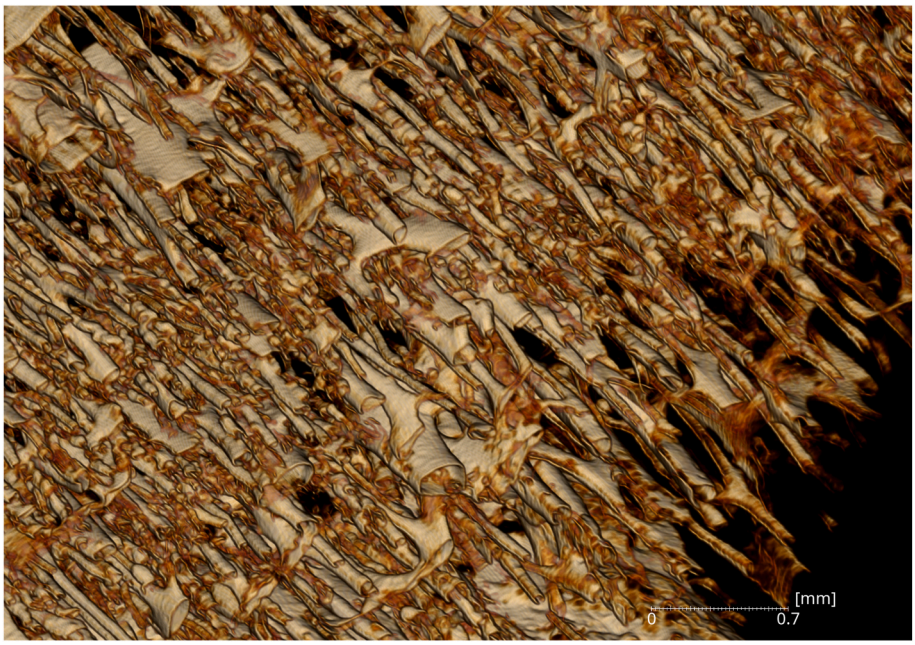

Fig. 7. 3D volume rendering with the "glow" colormap showing MFD tunneling in femoral sample GÖ01 (Göttlesbrunn).

renderings using the "glow" colormap. While it was still possible to apply the VHI to the virtual sections of sample S04 (Mandl et al., 2022 and Supplementary Material S17), a late-mature female in one of the regular inhumation graves of Asparn-Schletz, it was immediately clear that this individual was severely osteoporotic. The volume rendering using the "glow" colormap, of heavily demineralized samples such as S04, visualizes almost nothing (thus there is no volume image in Supplementary Material S17). Therefore, for heavily demineralized samples, or those characterized by pathological changes, it is worthwhile to try a variety of colormaps to test which can be used to best visualize canal structure and bioerosion in 3D.

5.5. Faunal samples

Again, although applying the VHI to non-human samples yielded similar ratings to the OHI (Mandl et al., 2022), they too were less clearly visualized in 3D. Little was visualized in faunal sample R04 (OHI 3.5/VHI 3) from the small sanctuary Object 12, District 1, at Roseldorf (Supplementary Material S18), tentatively identified as belonging to Artiodactyla, which is potentially due to the paucity of Haversian canals in bone of this mammalian order. Sample GÖ14 (OHI 3.5/VHI 4.25) (Supplementary Material S19), an ovicaprid humerus from Grave 14 at Göttlesbrunn, also yielded a poor volume rendering in which very little was visualized, consistent with both the SEM and virtual sections.

6. Conclusions

Unlike histological sections (or even virtual tomographic sections), the volume renderings of 3D images shown here are easy to produce and interpret, even for archaeologists inexperienced in bone histology, and readily facilitate the illustration and communication of microtaphonomic effects. Using a benchtop microCT scanner, intact bone samples 5–10 mm in diameter and 100–200 mm in length can be nondestructively imaged in high resolution (up to ~5 μm voxels) (Mandl et al., 2022), prior to their being subjected to other potentially more invasive treatments or analyses. Several fragments of bone (or, if small enough, an entire skeletal element) can be scanned at once or in automated batches. While scan acquisition may take some hours, once scanned and reconstructed, the entire sample can be rather quickly and easily visualized in 3D using a carefully chosen colormap that reduces the need for time-consuming segmentation. Furthermore, specimens do not require embedding, sectioning, and polishing, though samples that have already been embedded can be scanned without a resultant decrease in the clarity of the visualization of microanatomy. The method can thus be applied, for example, to old samples from museum collections without the need for further destructive sampling. To conclude, this method makes possible the visualization of bioerosion in a completely new way and at very high resolution.

Funding

This paper is part of a dissertation project and sponsored by the Vienna Doctoral School of Ecology and Evolution (VDSEE) 2021-Completion Grant of the University of Vienna awarded to K.M. Thin-section preparation was funded by the DEEPDEAD project (Deploying the Dead: Artefacts and Human Bodies in Socio-Cultural Transformations) under the HERA Joint Research Programme "Uses of the Past" (UP) [Collaborative Research Project (CRP) no. 15.055] and the European Union's Horizon 2020 research and innovation programme under grant agreement No. 649307.

Credit contributions

Kellie Sara Duffett Carlson: Conceptualization, Methodology, Software, Validation, Investigation, Data curation, Writing – original draft, Visualization, Project administration; Kirsten Mandl: Conceptualization, Methodology, Validation, Investigation, Data curation, Writing – original draft, Visualization, Project administration, Funding acquisition; Ashley McCall: Formal analysis, Writing – review & editing; David Brönnimann: Investigation, Resources; Maria Teschler-Nicola: Resources; Writing – review & editing; Estella Weiss-Krejci: Resources, Writing – review & editing, Funding acquisition; Brian Metscher: Methodology, Software, Validation, Writing – review & editing, Supervision, Project administration

Code availability

Not applicable.

Ethics approval

Not applicable.

Consent to participate

Not applicable.

Consent for publication

Not applicable.

Declaration of competing interest

The authors declare that they have no known competing financial interests or personal relationships that could have appeared to influence the work reported in this paper.

Acknowledgments

K.M. would like to thank Cordula Portmann, and especially Magdalena Müller-Gerbl, Peter Zimmermann, Mirelle Toranelli, and Andreas Ochsenbein from the Anatomy University Basel, Switzerland for training and support during thin-section preparation. Thanks are also extended to Maciej Karwowski, Jarosław M. Czubak, Michaela Fritzl, Franz Pieler, Veronika Holzer, Karin Wiltschke-Schrotta, and the Austrian Federal Monuments Office for providing the archaeological samples. E.W.-K. thanks Petra Goláňová for pointing out recent research on embalming in the Late Iron Age. We kindly thank Mihaela Pavličev for granting access to the microCT scanners at the Unit for Theoretical Biology in the Department for Evolutionary Biology at the University of Vienna. Scanning electron microscopy was performed at the Core Facility of Cell Imaging and Ultrastructure Research (CIUS), University of Vienna, member of the Vienna Life-Science Instruments; we therefore kindly thank Daniela Gruber and Siegfried Reipert. Thanks are extended to Irene Lichtscheidl and her team from the CIUS facility for her major support and for providing the light microscope. K.M. and K.S.D.C. would particularly like to thank Marishka, Lilly, and Grögar, without whom this paper would not be possible. We would like to thank Suzanne Freilich for comments and suggestions. K.S.D.C. would like to thank Ecne for their support; Lastly, we would also like to thank the anonymous reviewers for their comments.

Appendix A. Supplementary data

Supplementary data to this article can be found online at https://doi.org/10.1016/j.jas.2022.105646.

All original data are available in the online supplementary material. The tomographic images are archived at Zenodo (https://doi:10.5281/zenodo.6565553), publicly available under a Creative Commons Attribution 4.0 International (CC BY) license.

References

Aigouy, B., Mirouse, V., 2013. ScientiFig: a tool to build publication-ready scientific figures. Nat. Methods 10 (11), 1048. https://doi.org/10.1038/nmeth.2692.

Baier, W., Mangham, C., Warnett, J.M., Payne, M., Painter, M., Williams, M.A., 2019. Using histology to evaluate micro-CT findings of trauma in three post-mortem samples — first steps towards method validation. Forensic Sci. Int. 297, 27–34. https://doi.org/10.1016/j.forsciint.2019.01.027.

Balzer, A., Gleixner, G., Grupe, G., Schmidt, H.-L., Schramm, S., Turban-Just, S., 1997. In vitro decomposition of bone collagen by soil bacteria: the implications for stable isotope analysis in archaeometry. Archaeometry 39 (2), 415–429. https://doi.org/10.1111/j.1475-4754.1997.tb00817.x.

Bell, L.S., 1990. Palaeopathology and diagenesis: an SEM evaluation of structural changes using backscattered electron imaging. J. Archaeol. Sci. 17 (1), 85–102. https://doi.org/10.1016/0305-4403(90)90016-X.

Bell, L.S., Skinner, M.F., Jones, S.J., 1996. The speed of post mortem change to the human skeleton and its taphonomic significance. Forensic Sci. Int. 82, 129–140. https://doi.org/10.1016/0379-0738(96)01984-6.

Booth, T.J., 2016. An investigation into the relationship between bacterial bioerosion and funerary treatment in European archaeological human bone. Archaeometry 58 (3), 484–499. https://doi.org/10.1111/arcm.12190.

Booth, T.J., Chamberlain, A.T., Parker Pearson, M., 2015. Mummification in Bronze age britain. Antiquity 89 (347), 1155–1173. https://doi.org/10.15184/aqy.2015.111.

Booth, T.J., Redfern, R.C., Gowland, R.L., 2016. Immaculate conceptions: micro-CT analysis of diagenesis in Romano-British infant skeletons. J. Archaeol. Sci. 74, 124–134. https://doi.org/10.1016/j.jas.2016.08.007.

Boschin, F., Zanolli, C., Bernardini, F., Principalle, F., Tuniz, C., 2015. A look from the inside: microCT analysis of burned bones. Ethnobiol. Lett. 6 (2), 258–266. https://doi.org/10.14237/ebl.6.2.2015.365.

Bronnimann, D., Portmann, C., Pichler, S.L., Booth, T.J., Roder, B., Vach, W., Schibler, J., Rentzel, P., 2018. Contextualising the dead – combining geoarchaeology and osteoanthropology in a new multi-focus approach in bone histotaphonomy. J. Archaeol. Sci. 98, 45–58. https://doi.org/10.1016/j.jas.2018.08.005.

Burger, W., Burge, M.J., 2013. Principles of Digital Image Processing, Advanced Methods. Springer Press.

Caruso, V., Marinoni, N., Diella, V., Berna, F., Cantaluppi, M., Mancini, L., Trombino, L., Cattaneo, C., Pastero, L., Pavese, A., 2020. Bone diagenesis in archaeological and contemporary human remains: an investigation of bone 3D microstructure and minero-chemical assessment. Archaeol. Anthropol. Sci. 12, 162. https://doi.org/10.1007/s12520-020-01090-6.

Caruso, V., Marinoni, N., Diella, V., Possenti, E., Mancini, L., Cantaluppi, M., Berna, F., Cattaneao, C., Pavese, A., 2021. Diagenesis of juvenile skeletal remains: a multimodal and multiscale approach to examine the post-mortem decay of children's bones. J. Archaeol. Sci. 135, 105477 https://doi.org/10.1016/j.jas.2021.105477.

Child, A.M., 1995. Towards an understanding of the microbial decomposition of archaeological bone in the burial environment. J. Archaeol. Sci. 22 (2), 165–174. https://doi.org/10.1006/jasc.1995.0018.

Cooper, D.M.L., Turinsky, A.L., Sensen, C.W., Hallgrímsson, B., 2003. Quantitative 3D analysis of the canal network in cortical bone by micro-computed tomography. Anat. Rec. 274B, 169–179. https://doi.org/10.1002/ar.b.10024.

Dal Sasso, G., Maritan, L., Usai, D., Angelini, I., Artioli, G., 2014. Bone diagenesis at the micro-scale: bone alteration patterns during multiple burial phases at Al Khiday (Khartoum, Sudan) between the Early Holocene and the II century AD. Palaeogeogr. Palaeoclimatol. Palaeoecol. 416, 30–42. https://doi.org/10.1016/j.palaeo.2014.06.034.

Ellingham, S., Sandholzer, M.A., 2020. Determining volumetric shrinkage trends of burnt bone using micro-CT. J. Forensic Sci. 65 (1), 196–199. https://doi.org/10.1111/1556-4029.14150.

Fritzl, M.P., 2017. Die mehrfach belegten Gräber des Gräberfeldes von Inzersdorf ob der Traisen, NÖ. Unpublished MA thesis. University of Vienna.

Garland, A.N., 1987. A histological study of archaeological bone decomposition. In: Boddington, A., Garland, A.N., Janaway, R.C. (Eds.), Death, Decay and Reconstruction: Approaches to Archaeology and Forensic Science. Manchester University Press, pp. 109–126.

Ghezal, S., Ciesielski, E., Girard, B., Creuzieux, A., Gosnell, P., Mathe, C., Vieillescazes, C., Roure, R., 2019. Embalmed heads of the celtic Iron age in the south of France. J. Archaeol. Sci. 101, 181–188. https://doi.org/10.1016/j.jas.2018.09.011.

Grupe, G., Garland, A.N., 1993. Histology of Ancient Bone: Methods and Diagnosis. Springer.

Grupe, G., Dreses-Werringloer, U., 1993. Decomposition phenomena in thin-sections of excavated human bones. In: Grupe, G., Garland, A.N. (Eds.), Histology of Ancient Human Bone: Methods and Diagnosis. Springer, pp. 27–36.

Hackett, C.J., 1981. Microscopical focal destruction (tunnels) in exhumed human bones. Med. Sci. Law 21 (4), 243–265. https://doi.org/10.1177/002580248102100403.

Handschuh, S., Schwaha, T., Metscher, B.D., 2010. Showing their true colors: a practical approach to volume rendering from serial sections. BMC Dev. Biol. 10, 41. https://doi.org/10.1186/1471-213X-10-41.

Handschuh, S., Beisser, C.J., Ruthensteiner, B., Metscher, B.D., 2017. Microscopic dual-energy CT (microDECT): a flexible tool for multichannel ex vivo 3D imaging of biological specimens. J. Microsc. 267, 3–26. https://doi.org/10.1111/jmi.12543.

Hanson, M., Cain, C.R., 2007. Examining histology to identify burned bone. J. Archaeol. Sci. 34 (11), 1902–1913. https://doi.org/10.1016/j.jas.2007.01.009.

Hedges, R.E.M., Millard, A.R., Pike, A.W.G., 1995. Measurements and relationships of diagenetic alteration of bone from three archaeological sites. J. Archaeol. Sci. 22 (2), 201–209. https://doi.org/10.1006/jasc.1995.0022.

Hollund, H.I., Jans, M.M.E., Collins, M.J., Kars, H., Joosten, I., Kars, S.M., 2012. What happened here? Bone histology as a tool in decoding the postmortem histories of archaeological bone from Castricum, The Netherlands. Int. J. Osteoarchaeol. 22 (5), 537–548. https://doi.org/10.1002/oa.1273.

Holzer, V., 2009. Ergebnisse der bisherigen archäologischen Forschungen über die keltische Zentralsiedlung in Roseldorf/NÖ im Rahmen des Forschungsprojektes „Fürstensitz-Keltenstadt" Sandberg. In: Holzer, V. (Ed.), Roseldorf – Interdisziplinäre Forschungen zur größten keltischen Zentralsiedlung Österreichs. Österreichische Elektrizitätswirtschafts-Aktiengesellschaft, pp. 1–86 (Verbundgesellschaft).

Holzer, V., 2010a. Besonderheiten der Kultbezirke von Roseldorf in niederösterreich. Archäologie Österreichs 21 (1), 4–12.

Holzer, V., 2010b. Opfergrube, brunnen, heiligtum – grabungsergebnisse in Roseldorf 2010. Archäologie Österreichs 21 (2), 19–21.

Jackes, M., Sherburne, R., Lubell, D., Barker, C., Wayman, M., 2001. Destruction of microstructure in archaeological bone: a case study from Portugal. Int. J. Osteoarchaeol. 11 (6), 415–432. https://doi.org/10.1002/oa.583.

Jans, M.M.E., Nielsen-Marsh, C.M., Smith, C.I., Collins, M.J., Kars, H., 2004. The characterisation of microbial attack in archaeological bone. J. Archaeol. Sci. 31 (1), 87–95. https://doi.org/10.1016/j.jas.2003.07.007.

Jans, M.M.E., 2008. Microbial bioerosion of bone – a review. In: Wisshak, M., Tapanila, L. (Eds.), Current Developments in Bioerosion. Springer, pp. 397–413.

Karwowski, K., Czubak, J.M., 2019. Das latènezeitliche gräberfeld von Göttlesbrunn, flur geitzbilln (VF 07–08). In: Pieler, F., Trebsche, P. (Eds.), Beiträge zum Tag der Niederösterreichischen Landesarchäologie 2019. Wissenschaftliche Publikationen aus den Landessammlungen Niederösterreich, pp. 71–78.

Kendall, C., Høier Eriksen, A.M., Kontopoulos, I., Collins, M.J., Turner-Walker, G., 2018. Diagenesis of archaeological bone and tooth. Palaeogeogr. Palaeoclimatol. Palaeoecol. 491, 21–37. https://doi.org/10.1016/j.palaeo.2017.11.041.

Kontopoulos, I., Nystrom, P., White, L., 2016. Experimental taphonomy: post-mortem microstructural modifications in *Sus scrofa domesticus* bone. Forensic Sci. Int. 266, 320–328. https://doi.org/10.1016/j.forsciint.2016.06.024.

Le Garff, E., Mesli, V., Delannoy, Y., Colard, T., Demondion, X., Becart, A., Hedouin, V., 2017. Technical note: early post-mortem changes of human bone in taphonomy with μCT. Int. J. Leg. Med. 131, 761–770. https://doi.org/10.1007/s00414-016-1509-y.

Mandl, K., Duffett Carlson, K.S., Brönnimann, D., McCall, A., Grassberger, M., Teschler-Nicola, M., Weiss-Krejci, E., Metscher, B., 2022. Substantiating microCT for diagnosing bioerosion in archaeological bone using a new Virtual Histological Index (VHI). Archaeol. Anthropol. Sci. 14 (6), 104. https://doi.org/10.1007/s12520-022-01563-w.

Metcalf, J.L., Zech Xu, Z., Weiss, S., Lax, S., Van Treuren, W., Hyde, E.R., Jin Song, S., Amir, A., Larsen, P., Sangwan, N., Haarmann, D., Humphrey, G.C., Ackermann, G., Thompson, L.R., Lauber, C., Bibat, A., Nicholas, C., Gebert, M.J., Petrosini, J.F., Reed, S.C., Gilbert, J.A., Lynne, A.M., Bucheli, S.R., Carter, D.O., Knight, R., 2016. Microbial community assembly and metabolic function during mammalian corpse decomposition. Science 351 (6269), 158–162. https://doi.org/10.1126/science.aad2646.

Millard, A.M., 2001. The deterioration of bone. In: Pollard, A.M., Brothwell, D.R. (Eds.), Handbook of Archaeological Science. Wiley, pp. 633–643.

Moore, M.K., 2013. Functional morphology and medical imaging. In: DiGangi, E.A., Moore, M.K. (Eds.), Research Methods in Human Skeletal Biology. Academic Press, pp. 397–424. https://doi.org/10.1016/B978-0-12-385189-5.00014-5.

Parker Pearson, M., Chamberlain, A., Craig, O., Marshall, P., Mulville, J., Smith, H., Chenery, C., Collins, M., Cook, G., Craig, G., Evans, J., Hiller, J., Montgomery, J., Schwenninger, J.-L., Taylor, G., Weiss, T., 2005. Evidence for mummification in Bronze age britain. Antiquity 79, 529–546. https://doi.org/10.1017/S0003598X00114486.

Pieler, F., Teschler-Nicola, M., 2019. Asparn/Schletz: archäologische und anthropologische Bestandsaufnahme und Ausblick. In: Paper presented at the Conference of the West and South German Association for Archaeology and the Central and East German Association for Archaeology (02.04.2019) at Würzburg. Session: Mensch – Körper – Tod: Der Umgang mit menschlichen Überresten im Neolithikum. https://wsva.net/media/ag_neo_theorie_abstracts.pdf.

Piepenbrink, H., 1986. Two examples of biogenous dead bone decomposition and their consequences for taphonomic interpretation. J. Archaeol. Sci. 13 (5), 417–430. https://doi.org/10.1016/0305-4403(86)90012-9.

Rühli, F.J., Kuhn, G., Evison, R., Müller, R., Schultz, M., 2007. Diagnostic value of micro-CT in comparison with histology in the qualitative assessment of historical human skull bone pathologies. Am. J. Phys. Anthropol. 133 (4), 1099–1111. https://doi.org/10.1002/ajpa.20611.

Ryan, T.M., Sukhdeo, S., 2016. KSD-VP-1/1: analysis of the postcranial skeleton using high-resolution computed tomography. In: Haile-Selassie, Y., Su, D.F. (Eds.), The Postcranial Anatomy of Australopithecus Afarensis: New Insights from KSD-VP-1/1. Springer, pp. 39–62.

Scherf, H., 2013. Computed tomography in paleoanthropology — an overview. Archaeol. Anthropol. Sci. 5, 205–214. https://doi.org/10.1007/s12520-013-0128-5.

Schindelin, J., Arganda-Carreras, I., Frise, E., Kaynig, V., Longair, M., Pietzsch, T., Preibisch, S., Rueden, C., Saalfeld, S., Schmid, B., Tinevez, J.-Y., White, D.J., Hartenstein, V., Eliceiri, K., Tomancak, P., Cardona, A., 2012. Fiji: an open-source platform for biological-image analysis. Nat. Methods 9, 676–682. https://doi.org/10.1038/nmeth.2019.

Schroeder, W., Martin, K., Lorensen, B., 2018, fourth ed..1. The Visualization Toolkit: an Object-Oriented Approach to 3D Graphics. https://raw.githubusercontent.com/lorensen/VTKExamples/master/src/VTKBookLaTeX/VTKTextBook.pdf. (Accessed 20 April 2021).

Schultz, M., 1986. Die mikroskopische Untersuchung prähistorischer Skeletfunde: Anwendung und Aussagemöglichkeiten der differentialdiagnostischen Untersuchung, vol. 1. Archäologie und Museum, 6. https://www.archaeologie.bl.ch/uploads/files/website/Die_mikroskopische_Untersuchung_prahistorische_Skelet funde.pdf. (Accessed 8 October 2021).

Schultz, M., 2001. Paleohistopathology of bone: a new approach to the study of ancient diseases. In: Yearbook of Physical Anthropology, vol. 44, pp. 106–147. https://doi.org/10.1002/ajpa.10024.

Szombathy, J., 1929. Prähistorische Flachgräber bei Gemeinlebarn in Niederösterreich. De Gruyter & Co.

Szombathy, J., 1934. Bronzezeit-Skelette aus Niederösterreich und Mähren. Mittheilungen der Anthropologischen Gesellschaft in Wien 64, 1–101.

Teschler-Nicola, M., 2017. Komplexe Vielfalt – die menschlichen Relikte aus der latènezeitlichen Zentralsiedlung von Roseldorf und ihre archäothanatologische Evidenz. In: Pieler, F., Trebsche, P. (Eds.), Beiträge zum Tag der Niederösterreichischen Landesarchäologie 2017: Festschrift für Ernst Lauermann. Bösmüller Print Management GesmbH & Co. KG, pp. 248–261.

Thermo Scientific™, 2018. Thermo Scientific™ Amira™ Software 6: User's Guide. https://assets.thermofisher.com/TFS-Assets/MSD/Product-Guides/user-guide-amira-software.pdf. (Accessed 13 October 2020).

Tomasi, C., Manduchi, R., 1998. Bilateral filtering for gray and color images. In: Proceedings of the International Conference on Computer Vision, vol. 98. ICCV, Bombay, pp. 839–846. https://doi.org/10.1109/ICCV.1998.710815.

Trebsche, P., 2020. Kult, Deponierungen und Rituale. In: Trebsche, P. (Ed.), Keltische Münzstätten und Heiligtümer: Die jüngere Eisenzeit im Osten Österreichs (ca. 415 bis 50 v. Chr. Verlag der Österreichischen Akademie der Wissenschaften, pp. 440–465.

Tripp, J.A., Squire, M.E., Hamilton, J., Hedges, R.E.M., 2010. A nondestructive prescreening method for bone collagen content using micro-computed tomography. Radiocarbon 52, 612–619. https://doi.org/10.1017/S003382220004564.

Tripp, J.A., Squire, M.E., Hedges, R.E.M., Stevens, R.E., 2018. Use of micro-computed tomography imaging and porosity measurements as indicators of collagen preservation in archaeological bone. Palaeogeogr. Palaeoclimatol. Palaeoecol. 511, 462–471. https://doi.org/10.1016/j.palaeo.2018.09.012.

Turner-Walker, G., Jans, M., 2008. Reconstructing taphonomic histories using histological analysis. Palaeogeogr. Palaeoclimatol. Palaeoecol. 266 (3–4), 227–235. https://doi.org/10.1016/j.palaeo.2008.03.024.

Turner-Walker, G., 2012. Early bioerosion in skeletal tissues: persistence through deep time. Neues Jahrbuch für Geologie und Paläontologie 265 (2), 165–183. https://doi.org/10.1127/0077-7749/2012/0253.

Turner-Walker, G., 2019. Light at the end of the tunnels? The origins of microbial bioerosion in mineralised collagen. Palaeogeogr. Palaeoclimatol. Palaeoecol. 529, 24–38. https://doi.org/10.1016/j.palaeo.2019.05.020.

Walton, L.A., Bradley, R.S., Withers, P.J., Newton, V.L., Watson, R.E.B., Austin, C., Sherratt, M.J., 2015. Morphological characterisation of unstained and intact tissue micro-architecture by X-ray computed micro- and nano-tomography. Sci. Rep. 5, 10074 https://doi.org/10.1038/srep10074.

White, L., Booth, T.J., 2014. The origin of bacteria responsible for bioerosion to the internal bone microstructure: results from experimentally-deposited pig carcasses. Forensic Sci. Int. 239, 92–102. https://doi.org/10.1016/j.forsciint.2014.03.024.

Windl, H.J., 1998. Der Brunnen der Linearbandkeramik von Schletz/Asparn a. d. Zaya, p. B. Mistelbach, im Nordosten Österreichs. In: Koschik, H. (Ed.), Brunnen der Jungsteinzeit. Internationales Symposium in Erkelenz 27. – 29. Oktober 1997. Rheinland Verlag, pp. 85–93.

Windl, H.J., 2009. Zur Stratigraphie der bandkeramischen Grabenwerke von Asparn an der Zaya – Schletz. In: Zeeb-Lanz, A. (Ed.), Krisen – Kulturwandel – Kontinuitäten: Zum Ende der Bandkeramik in Mitteleuropa. Beiträge der internationalen Tagung in Herxheim 2007. Verlag Marie Leidorf, pp. 191–196.

Withers, P.J., Bouman, C., Carmignato, S., Cnudde, V., Grimaldi, D., Hagen, C.K., Maire, E., Manley, M., Du Plessis, A., Stock, S.R., 2021. X-ray computed tomography. Nat. Rev. Methods Prim. 1, 18. https://doi.org/10.1038/s43586-021-00015-4.

Yoshino, M., Kimijima, T., Miyasaka, S., Sato, H., Seta, S., 1991. Microscopical study on estimation of time since death in skeletal remains. Forensic Sci. Int. 49, 143–158. https://doi.org/10.1016/0379-0738(91)90074-s.